Time-Space Evolution of the Groningen Gas Field in Terms of b-Value: Insights and Implications for Seismic Hazard

Time-space evolution of the Groningen gas field in terms of b-value: insights and implications for seismic hazard.

Laura Gulia[1*]

[1] University of Bologna, Department of Physics and Astronomy, Bologna.

L. Gulia: Laura Gulia (laura.gulia@unibo.it)

Declaration of Competing Interests

The author acknowledges there are no conflicts of interest recorded

Abstract

The Groningen gas field, located in the north-east of Netherlands, is the Europe's largest onshore gas field. It was discovered in 1959 and production started in 1963: continuous production leads to reservoir compaction and subsidence, gradually loading pre-existing fault and induced seismicity started about 30 years into the production. The seismic hazard and risk related to the induced seismicity is determined not only the rate of activity, but it is equally influenced by the relative size distribution of the seismicity, the b-value. I re-analyze the spatial and temporal evolution of the b-value in the field using an alternative approach to overcome magnitude in completeness heterogeneity and link it to the evolution of fault loading and subsidence. Spatial variations of b-values are found to vary between 0.61 and 1.3, with lowest observed values observed in the location of the

2012 Huizinge M3.6 earthquake. In the last 10 years, the mapped b-value are more homogeneous throughout the field.

The spatial and temporal evolution of the b-value in the field is shown in this study to be quite complex and systematically linked it to the evolution of fault loading, absolute compaction and the rate of compaction, an important finding that offers new insights into hazard reduction and mitigation strategies of extraction relation induced seismicity. Compaction rates below 2 mm/year are not correlated to seismicity above M 2.0 in the history of the field, suggesting that low volume production may be safer than previously assumed.

Introduction

Anthropogenic activities lead to an increasing number of induced phenomena, including earthquakes. In the case of gas-production, extraction of mass and depletion of the pressure cause reservoir compaction, a process accompanied by both seismicity and surface subsidence (e.g., Segall, 1992; Zoback, 2007); these related processes show a delay with respect to gas extraction and the strict link between production, compaction and seismicity has been established in numerous studies (Bourne et al., 2014; Van Thienen-Visser and Fokker, 2017; Hol et al., 2018; Smith et al., 2019; Mehranpour et al., 2021).

The prime example of gas extraction related induced seismicity is the Groningen field in the Northwestern part of the Netherlands, the largest known gas field in the Western Europe and for many years the major supplier of natural gas to the Northwestern

European market (van Thiessen-Visser and Brunese, 2015). The gas is stored in the Permian Rotliegend sandstone, a shallow reservoir at a depth of about 3000 m, overlaid by a layer of Zechstein salt deposit (De Jager and Visser, 2017). The region is close to or even below sea level, thus surface subsidence, that has been measured already since one year after the beginning of gas production, is a substantial concern.

During production, mass is removed, fluid pressures are reduced, and the reservoir compacts; differential compaction rates gradually load pre-existing faults. About 1500 faults have been mapped so far from extensive 3D seismic surveys (NAM, 2016) and the predominant style-of-faulting of the field, derived from focal mechanisms (Willacy et al., 2019), is normal: gas extraction increases the effective vertical stress and thus the differential stress. Consequently, some faults can increasingly become unstable nucleating earthquakes: seismicity is indeed associated with the re-activation of normal faults, NW–SE trending, at reservoir level. Zbinden et al. (2017) provide a good review of the physical processes involved, including not only subsidence but also 2 phase flow between reservoir compartments and suggest three mechanism that influence the stress path that a fault undergoes during production:

1. The compaction of the reservoir leads to rotation of the principal stresses, which increases the shear stress in the fault zone.
2. The pressure drop in the gas reservoir strongly affects the horizontal and vertical stress acting on the fault through poroelastic effects, leading to an increase in differential stress and thus to an increase in shear stress.
3. Fluid flow into and out of the fault zone strongly affects the pore pressure evolution, hence altering the effective normal stress acting on the fault.

The induced seismicity related to the production causes considerable concern and anxiety in the population and increases the seismic risk in this previously almost a-seismic region: 1487 events with a maximum magnitude of Ml 3.6 have been recorded in the field from December 5, 1991, to May 22, 2022. The shallow surface in the area consists of thick layers of very soft deposits and the buildings have been designed and constructed without consideration for the horizontal loads typically experienced during an earthquake (van Elk et al., 2019): moderate magnitude events, such as the August 16, 2012, Huizinge Ml 3.6, can cause both significant non-structural damages to buildings and safety concerns for residents. Hazard and seismic risk assessment related to gas production became a priority in the following years.

One of the most important ingredients of hazard is the extrapolation of the observed frequency magnitude distribution, the b-value of the Gutenberg and Richter relationship (Gutenberg and Richter, 1944; Ishimoto and Ida, 1939), to larger magnitudes. It is one of the fundamental empirical laws of seismology and it estimates the number of earthquakes N larger than or equal to magnitude M, via the formula $\log(N) = a - bM$, whereby the *a-value* is a volume productivity measure, and the *b-value* quantifies the frequency-magnitude distribution (FMD) slope.

The b-value can be seen simply as an empirical fitting parameter that may be a constant, or variable with space and time. However, a wide body of research has documented that the changes in b-values are related to physics-based principles. Interpreting b-values in the physics-based framework can hence be a tool to better understand the reservoir evolution, it maybe also be the key to enhance the forecasting ability. A key concept is

the inverse correlation between b-value and differential stress, widely documented, both by laboratory specimens (from Scholz, 1968) and by observations in natural environments (Schorlemmer et al., 2005; Tormann et al., 2015; Gulia and Wiemer, 2010, 2019; Petrillo et al., 2020; Scholtz, 2015). For injections related induced seismicity Bachmann et al. (2012) and Goertz-Allman and Wiemer (2013) have shown that b-values in the highest pore pressures areas are much higher than observed at greater distances from the injection well. For natural seismicity, the stacking of the b-value time-series for 31 seismic sequences from well-monitored regions (Gulia et al., 2018) revealed a systematic b-value increase of about 20% in the proximity of the fault after a M6+; several single case studies (Papadopoulos et al., 2010; Tormann et al., 2015, 2014; Gulia and Wiemer, 2019, 2021; Gulia et al., 2016, 2020) investigated the b-value decreasing preceding the mainshock. All these findings are consistent with the inverse dependency of b-value with differential stress: the higher the applied differential stress, the lower the b value and vice versa.

In the case of Groningen, the b-value time-space variations should therefore reflect differential stress changes in the field that are driven by subsentence and compaction-generated stress-re-distribution. In this study, I first reconstruct the evolution in space and time of the b-value in the field and interpret it in terms of stress evolution. Finally, I reinvestigate, enrich, and discuss the correlation between compaction and b-value, first shown by Bourne et al. (2014).

Production and seismicity in the Groningen gas field

The Groningen gas field was discovered in 1959 and production started in 1963; the region was considered aseismic till 1991, when the first earthquake (Ml 2.3) occurred. Until 2003, seismicity was low and mainly located at the center of the field, the region where extraction was concentrated. Starting from 2003, due to the rising market demand, the production increased, and the number and magnitude of events started to increase too, till the occurrence of a Ml 3.6 event in 2012, that caused substantial non-structural damages and greatly increased the level of anxiety (Muntendam-Bos et al., 2017), together with the observed exponentially increasing trend in seismicity. Seismicity increased passing from 2 events with M>=1.5 events in 2001 to 29 events Ml>=1.5 in 2013 (Muntendam-Bos et al., 2021). Starting from 2014, after an investigation by the State Supervision of Mines (Muntendam-Bos and De Waal, 2013) that showed an increased risk for larger events due to gas extraction, production measures aimed at lowering the level of seismicity have been implemented and the production has been gradually reduced by 80% in the central part of the field and instead moved towards the South. The adopted measures appear to be successful, and they resulted in a reduction of the total number of events in the field: about 65% reduction of the seismicity rates in the center of the field (from 0.42 events km^2/yr in 2013 to 0.15 events km^2/yr in 2015), but an acceleration in the southwest (from 0.14 events km^2/yr in 2013 to 0.24 events km^2/yr in 2014; Muntendam-Bos, 2020). The expectation by the operator Nederlandse Aardolie Maatschappij BV (NAM) and regulator, the Dutch State Supervision of Mines (SodM), however, were that this reduction in seismicity would be a temporary relieve only, with continued production in the south, it was expected that the rate of seismicity would again increase. Despite the measures taken, a Ml 3.4 occurred near Zeerijp, NE part of the field, in January 2018. The continuing seismicity and the continued public opposition in the Groningen area notched the Dutch government to decide to further reduce gas

148 production, proposing a complete stop in 2030. This roadmap was further accelerated in
149 2020, and the termination of production has now been anticipated to 2023.
150
151 ***State of the art on b-value in the Groningen gas field***
152
153 ***Spatio-temporal variations of b-value -*** In the last decade, an increasing number of
154 papers investigated the effects of gas production on seismicity; among them, some
155 analysed the spatial and temporal variations of b-value. Below I summarise the key
156 findings of these studies.
157
158 The spatial variability of b-value have been investigated in a report by Harris and Bourne
159 (2015): they first show that the b-value of the overall catalogue is consistent with the
160 commonly accepted value of 1.0 for the period 1st May 1995 to 31st December 2014; then
161 they focus on two subregions of 5-km radius centred around two locations characterized
162 by different production – Loppersum and Ten Boer – finding that in the area around Ten
163 Boer the b-value is still consistent with 1, but in Loppersum, the subregion with the most
164 intense seismicity, it is significantly lower. To test whether significant temporal shifts are
165 present, each sub-catalogue is then divided in two parts of equal length and the b-values
166 of the two time periods compared. Till 2014, between the first and second halves of the
167 catalogues for the two sites, there are no temporal variations. b-value variations for
168 various periods and parts of the field have been confirmed by other studies (Wentinck,
169 2015; Bourne and Oates, 2017). Muntendam-Bos and Grobbe (2022) confirm the
170 statistically significant spatial variations of b-value but find no statistical evidence of a
171 temporal variation.
172

Muntendam-Bos et al. (2017) study whether both theory and models derived from observations of b-values in natural contexts could be adopted in hydrocarbon-production-induced seismicity. To answer this question, the authors analyse the temporal evolution of the b-value plotting the time-series of all the events recorded in the field, with different sample sizes; the spatial variability is not considered. Their plots show that before the occurrence of the biggest events in the field (2012), the b-value increases instead of decreasing: the consequent probability of a larger-magnitude event decreases before the occurrence of this quake. The authors conclude that *for short-term earthquake prediction by hydrocarbon-production-induced seismicity these types of analysis could be misleading*.

The Royal Netherlands Meteorological Institute (KNMI) progressed from simply monitoring the larger felt events to quantifying hazard and giving relevant input to exploration regulations (Dost et al., 2012). The probabilistic seismic hazard analysis conducted by KNMI (Dost and Spetzler, 2015; Spetzler and Dost, 2017) adopts a seismic source model based on recorded seismicity and performs an integration over seismic zones, following Cornell (1968). Due to the time-space b-value variations shown by Harris and Bourne (2015), different b-value were calculated for each seismic zone, that passed from four (Dost and Spetzler, 2015) to three (Spetzler and Dost, 2017).

b-value and compaction - Geodetic monitoring of subsidence over the field began in 1964 with optical levelling over a limited network in the central and southern part of the field (Bourne et al., 2014). In 1972, network coverage was extended to the entire field and the number of benchmarks increased; the subsidence rate accelerated after 1975 (van Thienen-Visser and Fokker, 2017). Bourne et al. (2014) superimposed the

198 epicentres of the events in the field on the reservoir compaction maps for different time
199 intervals and noted the concentration of events within the region of greatest compaction,
200 implying that the occurrence of earthquakes, in space and time, is influenced by the
201 reservoir compaction. The authors labelled each event according to the reservoir
202 compaction at the event's origin time and epicentre, then grouped subsets of events
203 within a range of compaction values, requiring a minimum number of 50 events. The
204 resulting plot (Figure 14 in Bourne et al., 2014) shows a compelling inverse correlation
205 between b-value and compaction. This correlation has important implications on the
206 future project of seismic hazard and risk and the forecasted decrease of the b-value with
207 increasing compaction, is a major driver of the seismic hazard in continued production.
208
209 ***Data***
210

211 The datasets used in this work are part of the data package provided by NAM to the
212 presenters at the Groningen Mmax Workshop II (Bommer and van Elk, 2017), held in
213 Amsterdam on June 2022, following the broad principles of the SSHAC (Senior Seismic
214 Hazard Analysis Committee) guidelines for hazard assessment. The seismic catalogue
215 contains 1487 events collected by the Royal Netherlands Meteorological Institute (KNMI)
216 in the period 5 December 1991- 22 May 2022; the original location of the KNMI seismic
217 stations have been converted from latitude and longitude to the standard system for The
218 Netherlands – RDS, expressed in terms of Easting and Northing coordinates (meters).
219 KNMI assumes a focal depth of 3km, which is the average depth of the gas reservoir.
220

221 The seismic network, fully operating since 1995, was designed to detect and locate
222 earthquakes of magnitude (Ml) 1.5 and larger (Dost et al., 2017); densification of the
223 monitoring network resulted in a decrease of the location threshold and magnitude of
224 completeness, that passed from 1.2 in the period April 2003-August 2012, to 0.8 in the
225 period August 2012-August 2014, reaching the current value of 0.5 since September 2014
226 (Dost et al., 2017; Paleja and Bierman, 2016). Since the network was not altered before
227 2010, the same Mc of 1.2 can be assumed also for the years preceding 2003 (Muntendam-
228 Bos, 2020). The compaction model for the field adopted in this work, included in the data
229 package provided by NAM, is calibrated on the V6 scenario, operational strategy 2 (OS2;
230 NAM 2021): the reservoir compaction is expressed as a function of both spatial position
231 and time since the start of production. Figure 1 shows a summary of the network
232 evolution with time.

233 ***Method and Results***

234

235 ***b-value changes: Radial analysis*** - To increase the robustness of the analysis, two
236 different methods to estimate b-values are used in this study: the first one is the formula
237 by Aki (1965), corrected by Utsu (1966) for binned magnitudes (from now on, AU66),
238 that relies on a robust and accurate estimate of the magnitude of completeness, Mc. As an
239 alternative method, the b-value estimator proposed by van der Elst (2021; from now on,
240 vde21) is also applied. The vde21 estimator does not require an accurate estimate of Mc
241 and allows to calculate b-value on datasets with a certain amount of incompleteness as
242 well as on datasets with variable levels of completeness in time. van per Elst (2021) shows
243 that the distribution of magnitude differences is identical to the distribution of magnitudes, but
244 with no reference to a minimum magnitude, and that the positive subset of the differences

between successive earthquakes is minimally biased by changing catalog completeness. This new estimator is insensitive to transient changes in catalog completeness and offers robust b-value estimations even during active earthquake sequences, (van der Elst, 2021) characterised by periods of strong incompleteness (Kagan, 2004).

The differential stresses on faults are changing substantially with space and time during production (e.g., Zbinden et al., 2017). Given the inverse correlation between b-value and differential stress, we should expect in the Groningen field both spatial and time variations of not only the activity rate (already well documented) but also of the b-value. The lowest b-values should be observed in the region of highest differential stress concentration, hence near the area where production was concentrated till 2014 and where also the largest event of Ml 36 has occurred. The highest b-values, in contrast, should be observed on the fringes of the fields. Such spatial variation should be time-dependent, reflecting gradually loading with time but also changes in the production: after 2014, when production is greatly reduced in the central part of the field and shifted southward, the b-values in the central part should remain constant and those in the surrounding areas should decrease. Figure 2 summarizes this conceptual expectation.

Because spatial and temporal variations of b-values are expected, but at the same time the dataset is very limited to resolve them, the choice of the right mapping approach is important. Spatial variations can be best evaluated by mapping b-value on a dense grid (Tormann et al., 2014), and robust estimations require typically a minimum number of 50 to 150 events above the magnitude of completeness (Wiemer and Wyss, 2000). Biases in b-value estimation also need to be carefully considered (Gulia et al., 2022; Gulia and

Wiemer, 2021); to also understand the temporal evolution, one would ideally investigate maps at different times.

To address the limits imposed by the size of the dataset while targeting the expected main gradients (Figure 2), I analyse first the seismicity in non-overlapping spherical volumes around the largest event (Huizinge, Ml 3.6 in 2012). I analyse two different periods, before and after the change in production in 2014, thus comparing the periods 01/1991-12/2013 and 01/2014- 05/ 2022. I sample events in the smallest radius that allows estimating a robust b-value, which corresponds to the volume containing a minimum number of 50 events above Mc. Considering the Mc established in previous work (Dost et al., 2017; Paleja and Bierman, 2016), the minimum radius for estimating b-values around the epicentre of the Huizinge event is about 4 km. Figure 3 shows the FMDs of the 4 doughnut-shaped volumes for the two time periods. In period 1, the b-value increase systematically from 0.61 for the central area, to b=1.3 for the outmost circle, events 12 – 20 km from the epicentre. For period 2, the central events show a similar b (0.67), but b-values of out segments have decrease considerably to values around 0.85. Figure 4 a-b summarizes the same observations, color-coded onto the theoretical scheme of Figure 2. The two plots in Figure 4 c-d compares the b-values as a function of distance calculated by AU66 and the ones estimated by vde21. Both shows the same trend and agree each other within the uncertainty, except for the volume 12-20 km, for which AU66 results in significantly higher estimates: this volume groups parts of the field, characterized by different levels of production, and the resulting b-value is probably derived from a heterogeneous sample. For the smallest volume (0-4 km) the sample size does not allow to estimate b-value by vde21.

b-value changes: Mapping - An alternative and less subjective approach to the radial analysis presented above is to map b-value on a dense spaced grid (1 km), selecting the events within a constant radius (5km), for the two significative time periods. Results are shown in Figure 5. For the first period, the lowest b-values (0.7-0.8) are found around the Huizinge epicentre, increasing with the distance, reaching values of about 1.2-1.3 in the outer parts. In the second period (2014-2022), the whole field exhibits more uniform values of about 0.8-0.9. Also in this case, the calculations have been performed by both AU66 (Figure 5 a-b) and vde21 estimator (Figure 5 c-d). These results are fully consistent with the radial sampling approach presented in Figure 3 and 4.

Maps of the differences in between the two periods are shown in Figure 6 (a, for AU66, and b, for vde21) are also consistent with the previous analysis. b-value generally increases in the North in period 2 and decrease in the South. For a direct comparison, I plot the FMDs in a 4-km radius around one grid node where the b-value remain constant (Figure 6c, grid node centred in the Huiginze epicentre) and two grid nodes with a marked decrease: one centred in the 2021 Ml 3.2 Garrelsweer event (Figure 6d, 4-km radius) and one in the South (Figure 6e, 5-km radius).

b-value changes: Temporal analysis - A continuous time series analysis of b-values adds to the analysis by not making assumptions on the analysis periods. To compute b-values with time, because the magnitude of completeness varies over time, I used the vde21 approach and calculate uncertainty with bootstrapping, choosing a constant number of events' approach to have robust and comparable estimations. Following the approach by Tormann et al. (2013), a window containing 120 events results in a good combination of robustness and time resolution, the window is then moved through the catalogue event

317 by event. Note that because the values are plotted at the time of the last event in the
318 subset, there will be independent estimates every 120 events; for the same reason, the
319 largest variations are visible with a delay, the length of which will depend on the time
320 interval required to have an independent sample. In this case, the expected variations
321 after production changes in 2014, will be shifted to the right part of the graph.

322

323 Two areas are analyzed separately in Figure 7: North and South of 593000. b-values in
324 the South (red line) are consistently higher, in line with the previous analysis. In addition,
325 the values in the South are more variable: b-values in the southern increase from 2010
326 onwards, while the ones in the Northern part (blue line) slightly decrease. After 2015, the
327 red line decreases sharply, continuing parallel but about 0.2 units higher than the blue
328 line until about 2021 when the two lines currently converge toward a common value. As
329 explained above, there is a delay in displaying changes due to the time length of the
330 sample.

331

332 ***b-value and compaction*** - Bourne at al. (2014; from now on, B2014) analyzed the
333 correlation between b-values and compaction in more detail, with the aim of forecasting
334 future seismicity and hence seismic hazard and risk based on the expected future
335 reservoir compaction. They first establish that 90% of the events with Ml≥ 1.5 occurred
336 at a time and place when the reservoir compaction was at least 0.18 implying that the
337 occurrence of earthquakes, in space and time, is strongly influenced by the reservoir
338 compaction. B2014 then directly compared compaction and b-value by applying an
339 innovative sampling approach: each event in the catalogue was labelled according to the
340 reservoir compaction at the event's time and epicentre. Then, subsets of at least 50 events

were selected within a range of compaction values and b-value estimates by AU66 and their 67% confidence intervals determined. The analysis indicated a statistically significant decrease in b-value with increasing compaction. The original figure by B2014 is shown here as inset in Figure 8a.

As a first step, I here reproduce and update the same plot for the same period (1991-2012; Figure 8a) used by B2024, and then analyse if the same corelation holds for the most recent data (2013-2022; Figure 8b) and for the entire catalogue (Figure 8c). I use a different compaction model NAM, 2021) and a constant compaction interval (± 5 cm) with respect to B2014, making the analysis more systematic: in the B2014 approach, subsets are not independent but strongly overlap with each other. The results in Figure 8 confirm the observations by B2014 for the period 1991 – 2012, and show that in the period 2013-2022, the dependence is even more pronounced, probably due to the improved quality and homogeneity of the available data with time. The FMDs of the maximum (b = 1.1) and minimum b-values (b = 0.79 and 0.7) for each time and compaction interval are also plotted in the frames d-f. The differences between the b-values are statistically highly significant, and the FMDs well adhere to a power law fit.

The B2014 approach samples events from all areas of the field, irrespective of location or time, destroying potential space-time information on the correlation of b-values and compaction. An alternative approach is to compare the compaction model, the seismicity and the b-value maps directly, using the same grid of the compaction data (0.5 km; Figure 9a). As noted by B2014, most induced earthquakes are concentrated in areas of higher compaction, and especially events with larger magnitudes, but there are also aseismic high compaction regions. Moreover, the very areas with the highest compaction values

366 are almost (dark red in the map). The epicentres of events at higher magnitudes seem to
367 contour this central patch; the same aseismic patches were already evident in the Figure
368 9 in B2014: the absolute compaction values between the two models are different but the
369 general trend is similar. The analysis confirms that earthquakes occur only in areas of
370 high compaction values, but some areas of high compaction, are aseismic.
371
372 To quantitatively correlate b-value and compaction, I determine b-values on sub-samples
373 composed by the events within a 5-km radius to each grid node, for the periods 1991-
374 2012 and 2013-2022 (Figure 9 b-c). In the first period (Figure 9b), b-value spans from
375 about 0.5 to 1.4 and no clear trend is visible in the compaction and b-value scatterplot.
376 After 2013 (Figure 9c), b-values in the field are more homogeneous, limited to the range
377 between 0.8 and 0.6; there is a weak anticorrelation between b-values and subsidence. In
378 an additional comparison that considers the spatial seismicity at a given time, I first
379 calculated the b-value for each event in the catalogue by selecting the 50 events closest
380 to the origin time of the event; this value was then compared to the compaction value of
381 the closest grid node at the origin time of the event: the results shown in Figure 9d do not
382 show a correlation.
383
384 ***b-values, magnitude and compaction rate*** - While b-values seem closely correlated to
385 compaction, an alternative hypothesis to investigate now is that b-values correlate with
386 compaction rate, thus strain rate, rather than absolute compaction or strain. Rate-
387 dependence has been proposed also as a mechanism to explain seismicity rate but has
388 not yet been correlated with b-values. To evaluate this correlation, differential
389 compaction is computed at every earthquake time, averaging over the last 10 year of
390 compaction values, and then b-values are computed for the nearest 50 events in space

prior to this time. The resulting clear correlation between b-values (y-axis) and compaction rate (x-axis) is shown in Figure 10a: b-values are lowest ($b < 0.8$) if compaction rates are exceeding about 0.4 cm/year.

Higher b-values then directly translate in a smaller chance of larger and potentially felt or damaging earthquakes. Figure 10b displays the correlation between compaction rates (x-axis), still in the last 10 years before the origin time, and the maximum observed magnitude (y-axis) in a 0.5-km cell centred on the compaction grid (NAM, 2021). Events above M2 occurred if the threshold of compaction rates of 0.28 cm/year is exceeded, events above M3 only once the compaction rates exceed 0.36 cm/year: the gray area in the upper left corner represents the magnitude-compaction-rate associations within which no seismicity is observed.

Implications for seismic hazard

For the first 30 years of gas production, no seismicity was observed in the field, but the continuous extraction led to the progressive reactivation of normal faults, and seismicity eventually started, reaching the maximum magnitude of 3.6 in 2012. While the link between seismic activity rate and production is well studied and widely accepted within the community (e.g., Segall, 1992; Zoback, 2007), the evolution of the average size distribution, the b-value, and production parameters are much less studied and disputed. This study adds in several relevant ways to the conceptual understanding of the seismicity in Groningen, but also to other depletion related induced seismicity. In doing so, the study also contributes to improving seismic hazard and risk assessment and to risk management strategies.

Unravelling the space and time evolution of the b-value is challenging, especially in area of sparse data. In the Groningen area, only 1487 induced earthquakes have been located so far since 1991, and only 637 above the estimate overall magnitude of completeness (Dost et al., 2017; Paleja and Bierman, 2016). This dataset is small, severely limiting the ability to resolve spatial and temporal patterns. This task is further complicated by the threat of biases in magnitudes, and by heterogeneity in magnitude reporting with space and time (e.g., Gulia et al., 2012; Tormann et al., 2010). The biggest challenging, however, is not data but process related: the stressing path these faults more than 1500 known (and countless more unknown) undergo is strongly depending on production parameters, which are variable with space and time. If indeed b-values are depending on the applied differential stresses as suggested from numerous studies (e.g., Schorlemmer et al., 2005), then one should expect a temporal and spatial evolution of b-values in the field. Even more complexity is added considering that the evolution of the shear stress on normal faults during compartmentalized depletion is non-linear if one also accounts for stress-dependent permeability and linear poroelasticity (Zbinden et al., 2017).

And indeed, the first contribution of this study is to establish firmly that such a pattern does exist and is well explained by theory. The b-values are lowest in the areas of highest compaction (Figure 3 and 4), and they change with time: increasing compaction in the Southern part of the field due to changes in the production pattern leads to decreases in b-values in these areas. I established these key findings using three different analysis approaches: concentric volumes focussed on the 2012 event hypocentre (Figures 3 and 4), spatial maps and differential b-value maps (Figures 5 and 6) and time-series analysis (Figure 7). I also use two different approaches to estimate b-values: AU66 and vde21.

Each mapping and method offer distinct advantages but also limitations, but the fact that all lead to broadly the same results strongly supports for the overall interpretation that b-values in the Groningen area are variable with space and time in a systematic and explainable way. These findings, obtained through the combined analysis of space and time as a function of production (field history in Figure 1), solidify and extend previous studies (Wentinck, 2015; Bourne and Oates, 2015; Muntendam-Bos et al., 2017). Note that method of van der Elst (2021) to estimate b-value has proven to be comparable, if not superior as an analysis tool.

The hazard implication of variable b-values is substantial: the probability of having an M 5 or larger in an area with a low b-value is thousands of times more than the probability of having the same event in an area with a high b-value. Of course, beside the b-value, the activity rate (a-value) needs to be estimated and considered also.

The change in differential stress that a steeply oriented boundary fault undergoes during 50 years of production is quite substantial, as demonstrated for example by Zbinden et. al. (2017). Differential stresses at reservoir depth increase from about 19.6 Mpa to value of 30.6 Mpa (base case) to 36 Mpa (case with multiple wells). The b-value changes of this doubling of differential stresses can be compared to past studies: Goertz-Allmann and Wiemer (2012) derived a b-value dependence on differential stress (Sd) for the Basel induced seismicity of b = −0.022* Sd, with a change in differential stress of 10 – 16 Mpa, we expect a decrease of the b-value of 0.22 to 0.35, comparable the observed range in this study. The b-value dependence on depth results in similar values (Spada et al., 2013; Scholz, 2015; Petruccelli et al., 2019), with observation showing that a doubling of the depth will reduce the b-value of crustal earthquakes on average by 0.2. Laboratory

studies are likewise in line with these observations: Goebel et al. (2013) for example report that a b-value change of about 0.3 – 0.4 is observed when progressing from 60% to 100% of the maximum strength of a fault. Therefore, the temporal and spatial changes observed here are well in line with the contemporary understanding of b-value. Given that hydro-geomechanical reservoir models of the Groningen area exist (van Wees et al., 2018; Bourne and Oates, 2017), it seems feasible to build models that are recreating the observations and using them to forecast future seismicity beyond empirical correlations.

One of the most striking results of this study is the very clear correlation of b-value and compaction, or compaction rate (Figure 9 and 10). B2014 had already proposed the inverse correlation between b-value and compaction in the field, here I confirm the findings by B2014 and extend the same analysis to 2022. Although I adopted a different, more updated compaction model from B2014, the observed correlations in the earlier period are in good agreement. More importantly, the correlation is maintained with the higher quality, recent data (Figure 8b). This striking correlation represents a major gradient in b-value, equal to the ones with depth (Spada et al., 2013), focal mechanism (Schorlemmer et al, 2005), mainshocks (Gulia et al., 2018) or pore pressure (Goertz-Allmann and Wiemer, 2013). All of these represent major gradients of differential stress in the Earth and are well explained in an ever more refined framework of b-value and differential stress correlations.

However, it is unclear (but important) at this point what exactly is responsible for the change in b-values, or what the best predictor of b-value evolution is: absolute compaction, compaction rate (so the temporal derivative of compaction at on place), or maybe compaction gradient (the spatial derivative of the compaction). Figures 9 and 10

suggest that all three are potential candidates, and of course all are related. The data are currently not able to distinguish between these hypotheses, but Figure 10b hints that compaction rates play a more important role in limiting larger magnitudes than absolute compaction: events with M>2 occur also at low absolute compaction (blue dots) but not at low compaction rates.

The fact that now the b-value in the North and in the South are now both equal and generally low is in terms of hazard perspective not ideal: switching production to the South has brought temporally relieve, by decreasing the rate of seismicity in the Loppersum area temporarily (Muntendam-Bos, 2020) and by increasing seismicity in an area of high b-value. But now the b-values in the South are equally low and continued production in any part of the field is likely to lower them further, suggesting that the seismic risk will continue to be substantial if production continues. I can only speculate that once production stops, b-value will also gradually increase as the stresses in the field are equalised.

In terms of risk mitigation strategies, the results presented in this study, when also combined with related models that forecast the seismicity, offer one potential avenue for continued exploitation of the field. The seismic risk is substantially lower while b-values are high, so Figure 9 and B2014 suggests that absolute compaction at any location should remain below 10 – 15 cm. This would also imply low seismicity rates but does not allow to produce any further in a majority of the field. If instead as suggested from this analysis shown in Figure 10b compaction rate is the driving mechanism, then a possible strategy would be to produce slowly and essentially everywhere, but not exceeding values of 0.2 – 0.3 cm of compaction per year. To better resolve this highly important issue that may allow continue production of gas in times of dire need, I suggest that an analysis of the

seismicity data based on a template-matched catalogue with a lower magnitude completeness, combined with geo-mechanical modelling of the stress dependent b-value may allow to add further support to the new idea of compaction rate driven b-values.

Data and Resources

Geomechanical, seismological, and geodetic data pertaining to the Groningen gas field: a data package used in the "Mmax II Workshop", on constraining the maximum earthquake magnitude in the Groningen field are available at https://public.yoda.uu.nl/geo/UU01/RHHRPY.html, DOI: 10.24416/UU01-RHHRPY

Acknowledgements

I gratefully acknowledge Jan van Elk, the Nederlandse Aardolie Maatschappij (NAM) and Julian Bommer for the Second Workshop on Mmax for Seismic Hazard and Risk Analysis in the Groningen Gas Field, Amsterdam, 13-17 June 2022 and for their support. I thank Onno van Wal and Stephen Bourne (Shell Global Solutions International B.V) for sharing data and Paolo Gasperini and Gianfranco Vannucci for their feedback on the manuscript. This study also benefits from the always stimulating discussions with Stefan Wiemer, especially on the correlation between b-value and compaction rates.

References

Aki, K. (1965). Maximum likelihood estimate of b in the formula logN = a − bM and its confidence limits, *Bull. Earthq. Res. Inst. Univ. Tokyo* 43, 237–239.

Bachmann, C., S. Wiemer, B. P. Goertz-Allmann, and J. Woessner (2012). Influence of pore-pressure on the event-size distribution of induced earthquakes, *Geophys. Res. Lett*. 39, no. 9, L09302, doi: 10.1029/2012GL051480.

Bommer, J.J. and J. van Elk (2017). Comment on "The Maximum Possible and the Maximum Expected Earthquake Magnitude for Production‐Induced Earthquakes at the Gas Field in Groningen, The Netherlands" by Gert Zöller and Matthias Holschneider. *Bull. Seism. Soc. Am.*; 107, no. 3: 1564–1567. doi: https://doi.org/10.1785/0120170040

Bourne, S. J., Oates S. J. (2017). Development of statistical geomechanical models for forecasting seismicity induced by gas production from the Groningen field, *Neth. J. Geosci* (96): s175-s182

Bourne, S. J., S. J. Oates, J. van Elk, and D. Doornhof (2014). A seismological model for earthquakes induced by fluid extraction from a subsurface reservoir, *J. Geophys. Res*. Solid Earth, 119, doi:10.1002/2014JB011663.

Cornell, C. A. (1968). Engineering seismic risk analysis, *Bull. Seismol. Soc. Am*. 58, no. 5, 1583–1606.

De Jager, J., and Visser, C. (2017). Geology of the Groningen field – an overview. *Netherlands* Neth. *J. Geosci, 96*, no. 5, S3-S15. doi:10.1017/njg.2017.22

559 Dost, B., Goutbeek, F., Eck, T.V. and Kraaijpoel,D. (2012). Monitoring induced seismicity
560 in the North of the Netherlands: status report 2010, *Tech. Rep*., Koninklijk Nederlands
561 Meteorologisch, de Bilt, The Netherlands.
562
563 Dost, B., and J. Spetzler (2015). Probabilistic seismic hazard analysis for induced
564 earthquakes in Groningen. KNMI report. Royal Netherlands Meteorological Institute (De
565 Bilt), 13.
566
567 Dost, B., E. Ruigrok, and J. Spetzler (2017). Development of probabilistic hazard
568 assessment for the Groningen gas field, Neth. *J. Geosci*., **96**, s235–s245.

569 Goebel, T. H. W., D. Schorlemmer, T. W. Becker, G. Dresen, and C. G. Sammis (2013).
570 Acoustic emissions document stress changes over many seismic cycles in stick-slip
571 experiments, *Geophys. Res. Lett*. 40, 2049–2054, doi: 10.1002/grl.50507.

572 Goertz-Allmann, B.P. and S. Wiemer (2013). Geomechanical modeling of induced
573 seismicity source parameters and implications for seismic hazard assessment. *Geophys.*;
574 78, no. 1: KS25–KS39. doi: https://doi.org/10.1190/geo2012-0102.1

575 Gulia, L., P. Gasperini and S. Wiemer (2022). Comment on "High‐Definition Mapping of
576 the Gutenberg‐Richter *b*‐Value and Its Relevance: A Case Study in Italy" by M. Taroni, J.
577 Zhuang, and W. Marzocchi. *Seism. Res. Lett.*, 93, no. 2A: 1089–1094.
578 doi: https://doi.org/10.1785/0220210159.
579

580 Gulia, L. and S. Wiemer (2021). Comment on “Two Foreshock Sequences Post Gulia and
581 Wiemer (2019)” by Kelian Dascher‐Cousineau, Thorne Lay, and Emily E. Brodsky. *Seism.*
582 *Res. Lett.*, 92, no. 5: 3251–3258. doi: https://doi.org/10.1785/0220200428.
583
584 Gulia, L., S. Wiemer, G. Vannucci (2020). Pseudoprospective Evaluation of the Foreshock
585 Traffic-Light System in Ridgecrest and Implications for Aftershock Hazard Assessment,
586 *Seismol. Res. Lett*. 91, no. 5, 2828–2842. doi https://doi.org/10.1785/0220190307
587
588 Gulia, L., and S. Wiemer (2019). Real-time discrimination of earthquake foreshocks and
589 aftershocks, *Nature* 574, 193–199.
590
591 Gulia, L., Rinaldi, A.P., Tormann, T., Vannucci, G., Enescu, B., and S. Wiemer (2018). The
592 effect of a mainshock on the size distribution of the aftershocks, *Geophys. Res. Lett.* 45,
593 doi: 10.1029/ 2018GL080619.
594
595 Gulia, L., Tormann, T., Wiemer, S., Herrmann, M., and S. Seif (2016). Short-term
596 probabilistic earthquake risk assessment considering time dependent b values. *Geophys.*
597 *Res. Lett.*, 43, 1100–1108. https://doi.org/10.1002/2015GL066686
598
599 Gulia, L., S. Wiemer, and M. Wyss (2012). Catalog artifacts and quality controls,
600 community online resource for statistical seismicity analysis, doi: 10.5078/corssa-
601 93722864.
602

Gulia, L., and S. Wiemer (2010). The influence of tectonic regimes on the earthquake size distribution: A case study for Italy. Geophys. Res. Lett, 37, L10305. https://doi.org/10.1029/2010GL043066

Gutenberg, B., and C.F. Richter (1944). Frequency of earthquakes in California. *Bull. Seismol. Soc. Am.*, 34, 185–188

Harris, C.K., and S. Bourne (2015). Maximum Likelihood Estimates of b-Value for Induced Seismicity in the Groningen Field, Restricted Draft Report, https://www.sodm.nl/documenten/publicaties/2015/06/23/6.-maximum-likelihood-estimates-of-b-value-for-induced-seismicity-in-the-groningen-field-c.k.-harris--s.j.-bourne-restricted-draft-report-1-mei-2015.

Hol, S., A., van der Linden, S., Bierman, S. Marcelis, A. Makurat (2018). Rock Physical Controls on Production-induced Compaction in the Groningen Field. *Sci. Rep.,* 8, 7156. https://doi.org/10.1038/s41598-018-25455-z

Ishimoto, M., and K. Iida (1939). Observations sur les séismes enregistrés par le microséismographe construit dernièrement, *Bull. Earthq. Res. Inst*. 17, 443–478 (in French).

Mehranpour, M. H., Hangx, S. J. T., and C.J. Spiers (2021). Compaction of the Groningen gas reservoir sandstone: Discrete element modeling using microphysically based grain- scale interaction laws. J. *Geophys. Res.: Solid Earth*, *126*, e2021JB021722. https://doi. org/10.1029/2021JB021722

Muntendam-Bos, A.G., and N. Grobbe (2022). Data-driven spatiotemporal assessment of the event-size distribution of the Groningen extraction-induced seismicity catalogue. *Sci. Rep.,* 12**,** 10119 (2022). https://doi.org/10.1038/s41598-022-14451-z

Muntendam-Bos, A.G. (2020) Clustering characteristics of gas-extraction induced seismicity in the Groningen gas field, *Geophys. J. Int.*, 221, no. 2, 879–892, https://doi.org/10.1093/gji/ggaa038

Muntendam-Bos, A.G., Roest, J.P.A. and H.A. de Waal (2017). The effect of imposed production measures on gas extraction induced seismic risk. In: Netherlands *J. Geosc*. 96.5, s271–S278.

Muntendam-Bos, A.G., and J.A. de Waal (2013). Reassessment of the probability of higher magnitude earthquakes in the Groningen gas field. SodM (National Mines Inspectorate) report: 33 pp. Open access via https://www.rijksoverheid.nl/documenten/rapporten/2013/01/16/ reassessment-of-the-probability-of-higher-magnitude-earthquakes-in-thegroningen-gas-field.

NAM (2016). Winningsplan Groningen Gasveld 2016. Nederlandse Aardolie Maatschappij BV (Assen). Available at www.nam.nl/feiten-en-cijfers/gaswinning.html.

651 NAM (2021). Groningen long term subsidence forecast, EP202008201822, https://nam-
652 onderzoeksrapporten.data-app.nl/reports/download/groningen/en/d8970d78-f51a-
653 4a3b-85d4-f80f42d055af
654
655 Paleja, R., Bierman, S. and M. Jones (2016). Impact of production shut-in on interevent
656 time in Groningen. A statistical perspective. Shell report. Royal Dutch Shell (The Hague):
657 35pp. Available at www.nam.nl/feiten-en-cijfers.
658
659 Papadopoulos, G. A., Charalampakis, M., Fokaefs, A., and G. Minadakis, (2010). Strong
660 foreshock signal preceding the L'Aquila (Italy) earthquake (Mw 6.3) of 6 April 2009. *Nat.*
661 *Hazards Earth Syst. Sc.,* 10, no. 1, 19–24. https://doi.org/10.5194/nhess-10-19-2010
662
663 Petrillo, G., Lippiello, E., Landes, F.P., A. Rosso (2020). The influence of the brittle-ductile
664 transition zone on aftershock and foreshock occurrence. *Nat. Commun.* 11, 3010.
665 https://doi.org/10.1038/s41467-020-16811-7
666
667 Petruccelli, A., P. Gasperini, T. Tormann, D. Schorlemmer, A. P. Rinaldi, G. Vannucci, and S.
668 Wiemer (2019). Simultaneous dependence of the earthquake-size distribution on
669 faulting style and depth, *Geophys. Res. Lett*. 46, no. 20, 11044–11053, doi:
670 10.1029/2019GL083997
671
672 Segall, P. (1992). Induced stresses due to fluid extraction from axisymmetric
673 reservoirs. *Pure Appl. Geophys.*, 139, no. 3/4: 535–560.
674

675 Scholz, C. H. (1968). The frequency-magnitude relation of microfracturing in rock and its
676 relation to earthquakes, *Bull. Seismol. Soc. Am*. 58, 399–415.
677
678 Scholz, C.H. (2015). On the stress dependence of the earthquake b value, *Geophys. Res.*
679 *Lett.*, 42, 1399–1402, doi: 10.1002/2014GL062863.
680
681 Schorlemmer D., S. Wiemer and M. Wyss (2005). Variations in earthquake-size
682 distribution across different stress regimes. *Nature,* 437(7058), 539–542.
683 https://doi.org/10.1038/nature04094
684
685 Shi, Y., and B. Bolt (1982). The standard error of the magnitude frequency b value, *Bull.*
686 *Seismol. Soc. Am*. 72, no. 5, 1677–1687.
687
688 Smith, J. D., Avouac, J.-P., White, R. S., Copley, A., Gualandi, A., and S. Bourne (2019).
689 Reconciling the long-term relationship between reservoir pore pressure depletion and
690 compaction in the Groningen region. J. Geophys. Res.: Solid Earth, 124,6165–6178.
691 https://doi.org/10.1029/2018JB016801
692
693 Spada, M., Tormann, T., Wiemer, S., and B. Enescu (2013). Generic dependence of the
694 frequency-size distribution of earthquakes on depth and its relation to the strength
695 profile of the crust. *Geophys. Res. Lett.*, 40, no. 4, 709–714.
696 https://doi.org/10.1029/2012GL054198

Tormann, T., S. Wiemer, A. Mignan (2014). Systematic survey of high-resolution b value imaging along Californian faults: Inference on asperities, *J. Geophys. Res*, 119, no. 3, 2029-2054, https://doi.org/10.1002/2013JB010867

Tormann, T., Enescu, B., Woessner, J. and S. Wiemer (2015). Randomness of megathrust earthquakes implied by rapid stress recovery after the Japan earthquake. *Nat. Geosci*. 8, 152–158.

Tormann T., S. Wiemer, and E. Hauksson (2010), changes in reporting Rates in the Southern California Earthquake Catalog, Introduced by a New Definition of Ml, *Bull. Seism. Soc. Am*. 100, no. 4, 1733{1742

Utsu, T. (1966). A statistical significance test of the difference in b-value between two earthquake groups, *J. Phys. Earth*, 14, 34-40.

van der Elst, N. J. (2021). B-positive: A robust estimator of aftershock magnitude distribution in transiently incomplete catalogs. *J. Geophys. Res.: Solid Earth*, 126, e2020JB021027. https://doi.org/10.1029/2020JB021027

Van Elk, J., Bourne, S. J., Oates, S.J., Bommer, J.J., Pinho, R. and H. Crownley (2019). A Probabilistic Model to Evaluate Options for Mitigating Induced Seismic Risk. *Earthq. Spectra*, 35, no. 2, 537-564. doi:10.1193/050918EQS118M

van Thienen-Visser, K., and J. N. Breunese (2015). Induced seismicity of the Groningen gas field: History and recent developments: *Lead. Edge*, 34, 664–671, doi: 10.1190/tle34060664.1.

Van Thienen-Visser, K., and P. Fokker (2017). The future of subsidence modelling: Compaction and subsidence due to gas depletion of the Groningen gas field in the Netherlands. *Neth. J. Geosci*., 96, no. 5, S105-S116. doi:10.1017/njg.2017.10

van Wees, J.D., S. Osinga, K. van Thienen-Visser, P. A Fokker (2018). Reservoir creep and induced seismicity: inferences from geomechanical modeling of gas depletion in the Groningen field, *Geophys. J. Int.*, 212, no. 3, 1487–1497, https://doi.org/10.1093/gji/ggx452

Wentinck, H.M. (2015), Induced seismicity in the Groningen field - statistical assessment of tremors along faults in a compacting reservoir, Shell Global Solutions International B.V., Rijswijk, Internal Report, 183 pp.

Willacy, C. van Dedem E., Minisini S., Li J., Blockland J.W., Das I. and A. Droujinine (2017). Full-waveform event location and moment tensor inversion for induced seismicity. *Geophys.*, 84, no. 2, KS39–KS47. https:// doi. org/ 10. 1190/ GEO20 18- 0212.1.

Zbinden, D., A. P. Rinaldi, L. Urpi, and S. Wiemer (2017). On the physics-based processes behind production-induced seismicity in natural gas fields, *J. Geophys. Res. Solid Earth*, 122,3792–3812, doi:10.1002/2017JB014003.

744 Zoback, M. D. (2007). Reservoir geomechanics: Cambridge University Press.
745 https://doi.org/10.1017/CBO9780511586477

746

747 ***Author's mailing address***

748 laura.gulia@unibo.it

749

750 ***List of Figures and Captions***

751

752 Figure 1 –***Field history***: essential steps and significant time-intervals in the Groningen
753 gas field since the start in gas production. Note that time is not scaled.

754

755 Figure 2 – ***Expected b-values*** - Theoretical and expected b-value in the field for two
756 significant time periods according to the current literature on b-value: on the left) the
757 lowest b-value are expected in the central part of the field, surrounded by higher values
758 during the period of high production; on the right) decreasing b-values are expected in
759 the outer part of the field due to the shift in production started in 2014.

760

761 Figure 3 –***b-value in doughnut-shaped spherical volumes*** - a) Seismicity in the field
762 colored according to the distance from the epicentre of the 2012 Ml 3.6 event in Huizinge;
763 b-c: frequency-magnitude distributions of the 4 volumes in frame (a) for the two periods
764 under examination: before 2014 (b) and after (c). In the first period, the b-value increases
765 with the distance from the Huiginze epicentre; in the second period, the values are more
766 homogeneous.

Figure 4 – ***Observed b-values*** - a-b) b-value in spherical volumes from the epicentre of the 2012 Ml 3.6 event in Huizinge: in the period 1991-2014, the b-value increases with the distance (a); after 2014, the b-value is more homogeneous, tending to a common value (b); c-d) comparison between the b-value estimated by AU66 (blu dots; uncertainty by Shi and Bolt, 1982) and the ones calculated on the same dataset by vde21 (red dots, uncertainty by bootstrapping) before 2014 (c) and after (d).

Figure 5 – ***Spatial evolution of b-value in time*** - b-value maps for the periods 1991-2013 and 2014-2022; a,b) maps calculated by AU66 and Mc from Dost et al. (2018) and Paleja and Bierman (2016); c-d) by vde21. The epicentres of the biggest events in the two periods are also shown.

Figure 6 – ***FMDs in significative volumes*** - a) maps of the differences between the two b-value maps in Figure 6 a-b; b) maps of the differences between the two b-value maps in Figure 6 c-d; c-e) comparison between the frequency-magnitude distributions of the b-value by AU66 for 3 locations (Huiginze, Garrelsweer and a grid node in the South, black dot in maps a-b) in the time periods 1991-2013 and 2014-2022.

Figure 7 – ***b-value time-series*** - b-value time-series for all the events North of 593000 (blue line) and South of 593000 (red line) estimated by vde21, uncertainty by bootstrap (shaded colors). The two lines currently seems to converge toward a common value. The most important steps of the field history shown in Figure 1 are marked on the x-axis.

Figure 8 – ***b-value and compaction*** - a-c) b-value estimated by AU66 following B2014 on subsets of at least 50 events within the range ± 5 cm of compaction values, for the periods 1991-2012 (a), 2013-2022 (b) and for the entire period (1991-2022, c). The original figure 14 by B2014 is shown as inset in a.

d-f) comparison between the frequency-magnitude distributions of the minimum and maximum b-value for the same periods.

Figure 9 – ***Compaction map and b-value*** - a) compaction map: cumulative compaction at the year 2022, calibrated on the V6 scenario, operational strategy 2 (OS2; NAM 2021) on a grid of 0.5 km with superimposed seismicity from 1991 to May 2022; b-c) b-value versus compaction for the same 0.5-km spaced grid for the periods 1991-2012 and 2013-2022. Vertical bar: uncertainty by Shi and Bolt (1982); d) b-value calculated for each event in the catalog sampling the closest 50 event above Mc at the origin time versus the compaction of the closest grid node. Vertical bar: uncertainty by Shi and Bolt (1982).

Figure 10 – ***b-value, magnitude, and compaction rates*** - a) Correlation between b-value and compaction rates, expressed by the difference in compaction in 10 years before the event's origin time. Vertical bar: uncertainty by Shi and Bolt (1982); black solid line: linear regression modelling the relationship between b-value and difference in compaction (b=-0.0424x+1.067); b) correlation between the maximum magnitude for each 0.5 km cell and compaction rates, expressed by the difference in compaction in 10 years before the event's origin time, color-coded with respect to the absolute compaction. Gray area: if production does not result in the exceedance of about 0.35 cm of compaction per year, events above M3 do not occur.

816 ***Figures with captions***

817

818

819

820

821

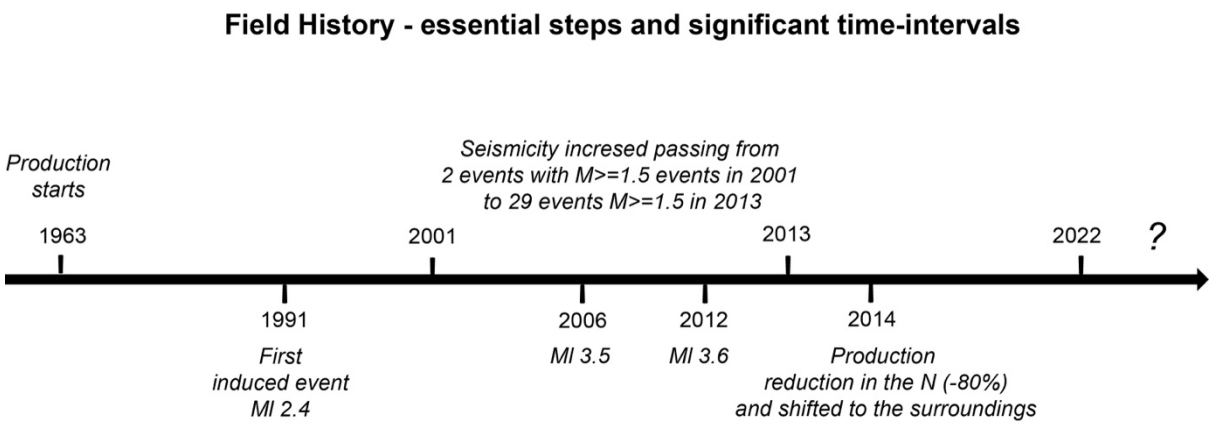

822

823

824 Figure 1 –***Field history***: essential steps and significant time-intervals in the Groningen

825 gas field since the start in gas production. Note that time is not scaled.

826

827

828

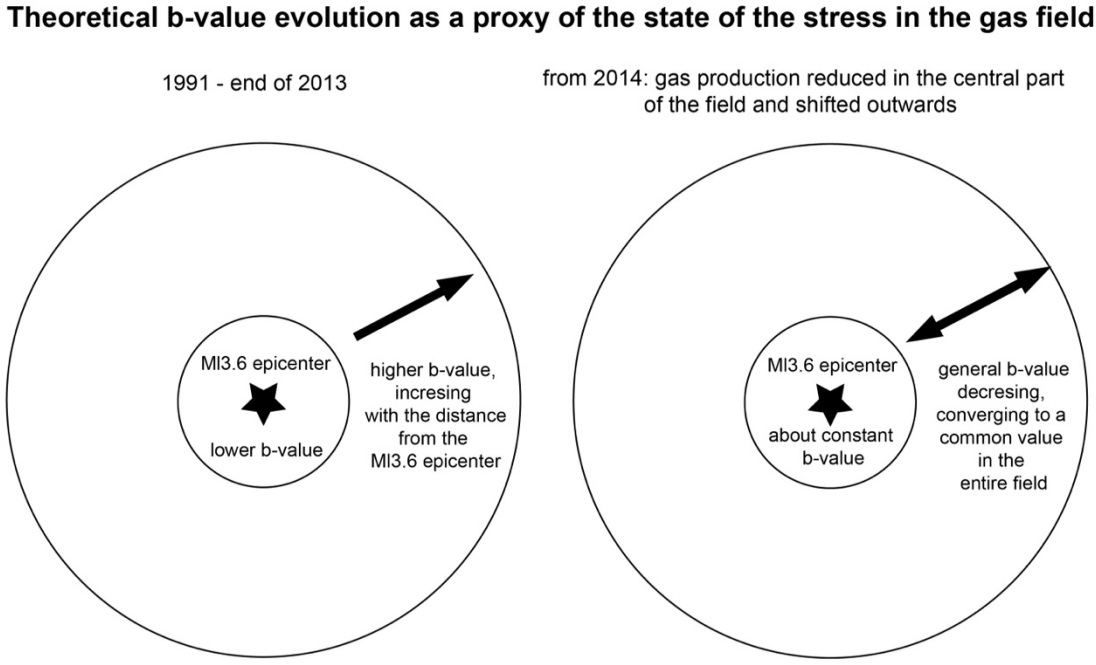

829

830

831 Figure 2 – ***Expected b-values*** - Theoretical and expected b-value in the field for two
832 significant time periods according to the current literature on b-value: on the left) the
833 lowest b-value are expected in the central part of the field, surrounded by higher values
834 during the period of high production; on the right) decreasing b-values are expected in
835 the outer part of the field due to the shift in production started in 2014.

836

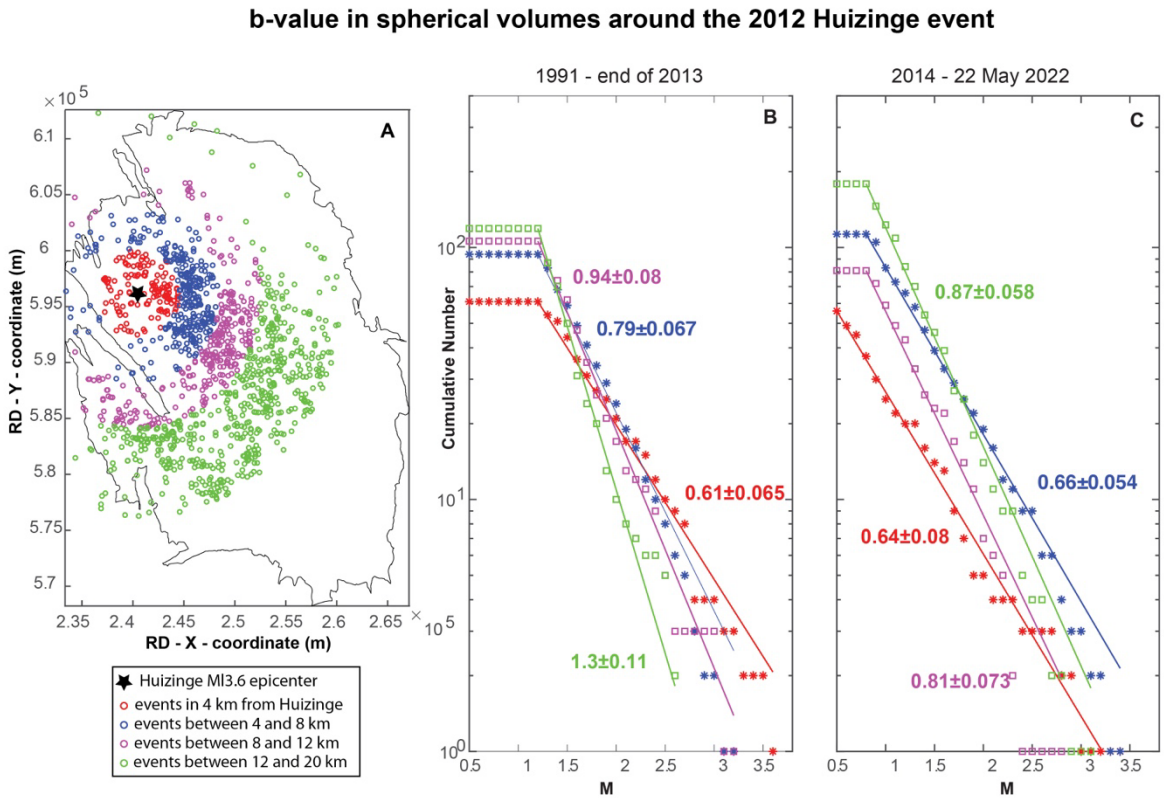

837

838

839 Figure 3 –***b-value in doughnut-shaped spherical volumes*** - a) Seismicity in the field
840 colored according to the distance from the epicentre of the 2012 Ml 3.6 event in Huizinge;
841 b-c: frequency-magnitude distributions of the 4 volumes in frame (a) for the two periods
842 under examination: before 2014 (b) and after (c). In the first period, the b-value increases
843 with the distance from the Huiginze epicentre; in the second period, the values are more
844 homogeneous.

845

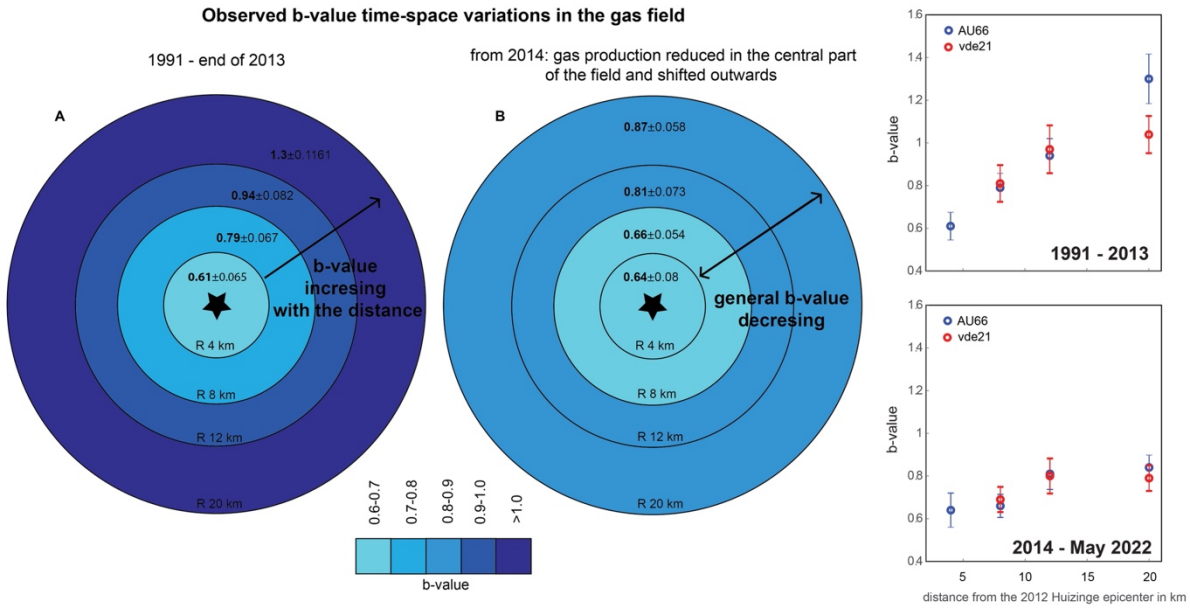

846

847 Figure 4 – ***Observed b-values*** - a-b) b-value in spherical volumes from the epicentre of
848 the 2012 Ml 3.6 event in Huizinge: in the period 1991-2014, the b-value increases with
849 the distance (a); after 2014, the b-value is more homogeneous, tending to a common
850 value (b); c-d) comparison between the b-value estimated by AU66 (blu dots; uncertainty
851 by Shi and Bolt, 1982) and the ones calculated on the same dataset by vde21 (red dots,
852 uncertainty by bootstrapping) before 2014 (c) and after (d).

853

854

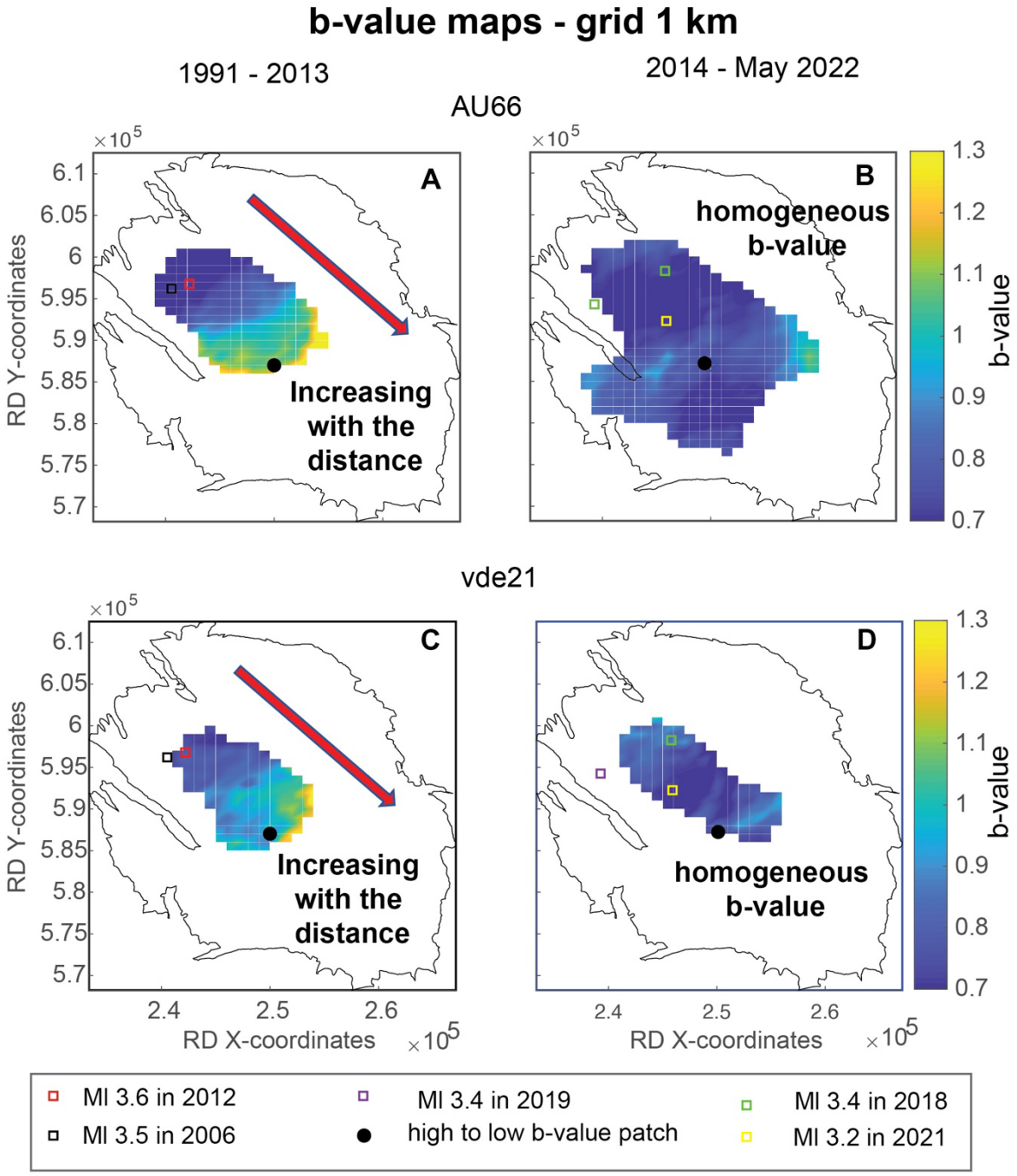

855

856 Figure 5 – ***Spatial evolution of b-value in time*** - b-value maps for the periods 1991-2013
857 and 2014-2022; a,b) maps calculated by AU66 and Mc from Dost et al. (2018) and Paleja
858 and Bierman (2016); c-d) by vde21. The epicentres of the biggest events in the two
859 periods are also shown.

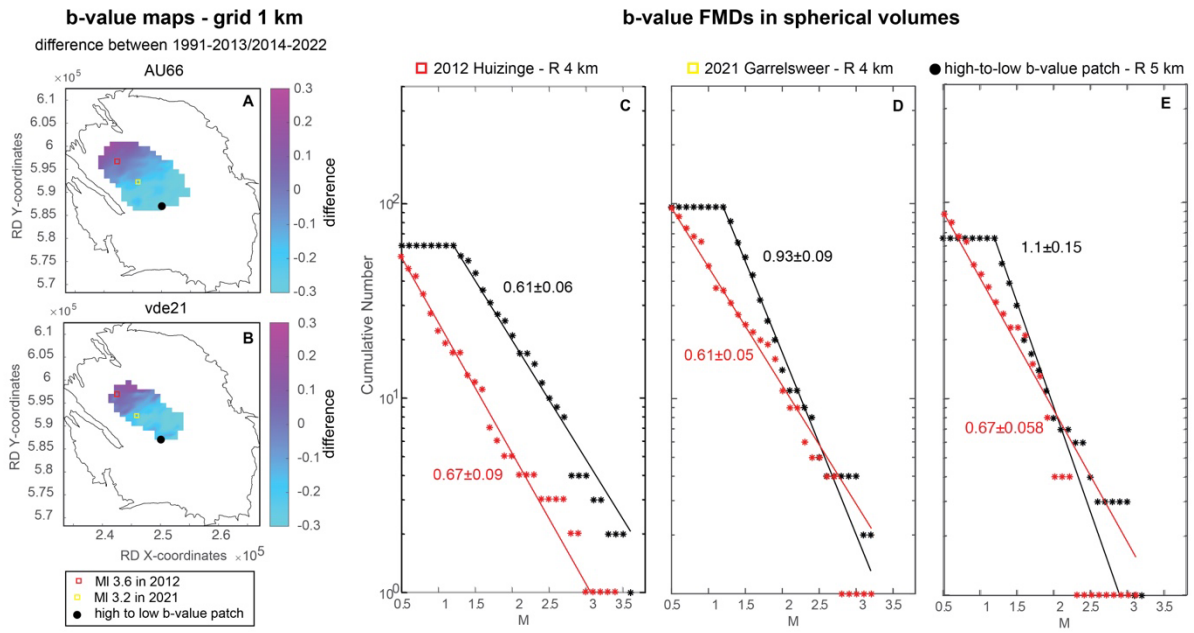

860

861 Figure 6 – ***FMDs in significative volumes*** - a) maps of the differences between the two b-
862 value maps in Figure 6 a-b; b) maps of the differences between the two b-value maps in
863 Figure 6 c-d; c-e) comparison between the frequency-magnitude distributions of the b-
864 value by AU66 for 3 locations (Huiginze, Garrelsweer and a grid node in the South, black
865 dot in maps a-b) in the time periods 1991-2013 and 2014-2022.

866

867

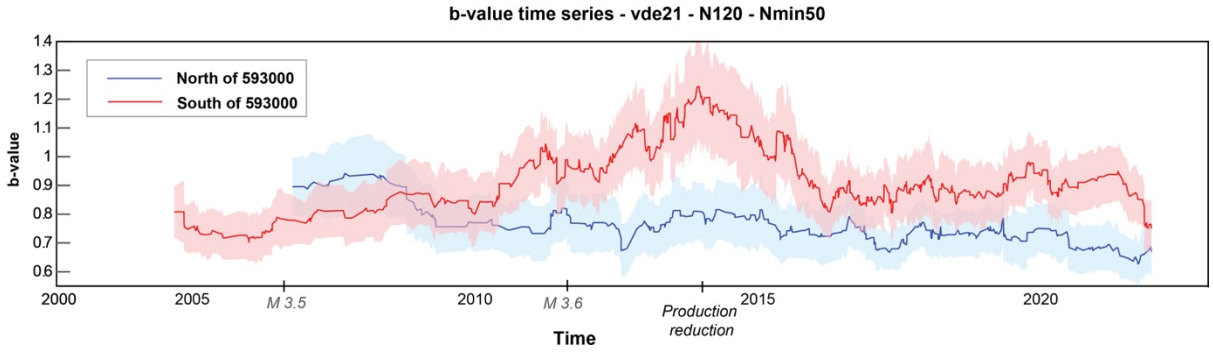

868

869

870 Figure 7 – ***b-value time-series*** - b-value time-series for all the events North of 593000
871 (blue line) and South of 593000 (red line) estimated by vde21, uncertainty by bootstrap
872 (shaded colors). The two lines currently seems to converge toward a common value. The
873 most important steps of the field history shown in Figure 1 are marked on the x-axis.

874

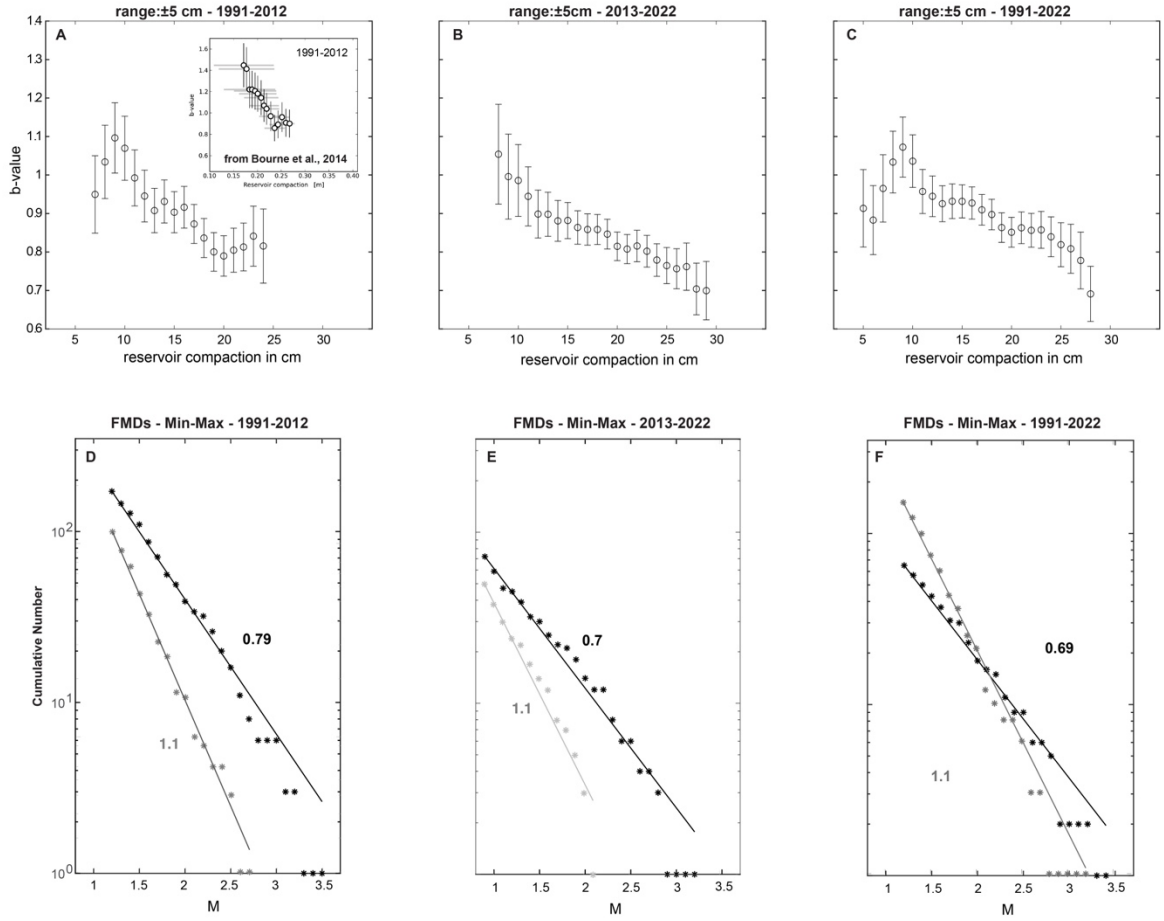

875

876

877 Figure 8 – ***b-value and compaction*** - a-c) b-value estimated by AU66 following B2014 on
878 subsets of at least 50 events within the range ± 5 cm of compaction values, for the periods
879 1991-2012 (a), 2013-2022 (b) and for the entire period (1991-2022, c). The original
880 figure 14 by B2014 is shown as inset in a.
881 d-f) comparison between the frequency-magnitude distributions of the minimum and
882 maximum b-value for the same periods.

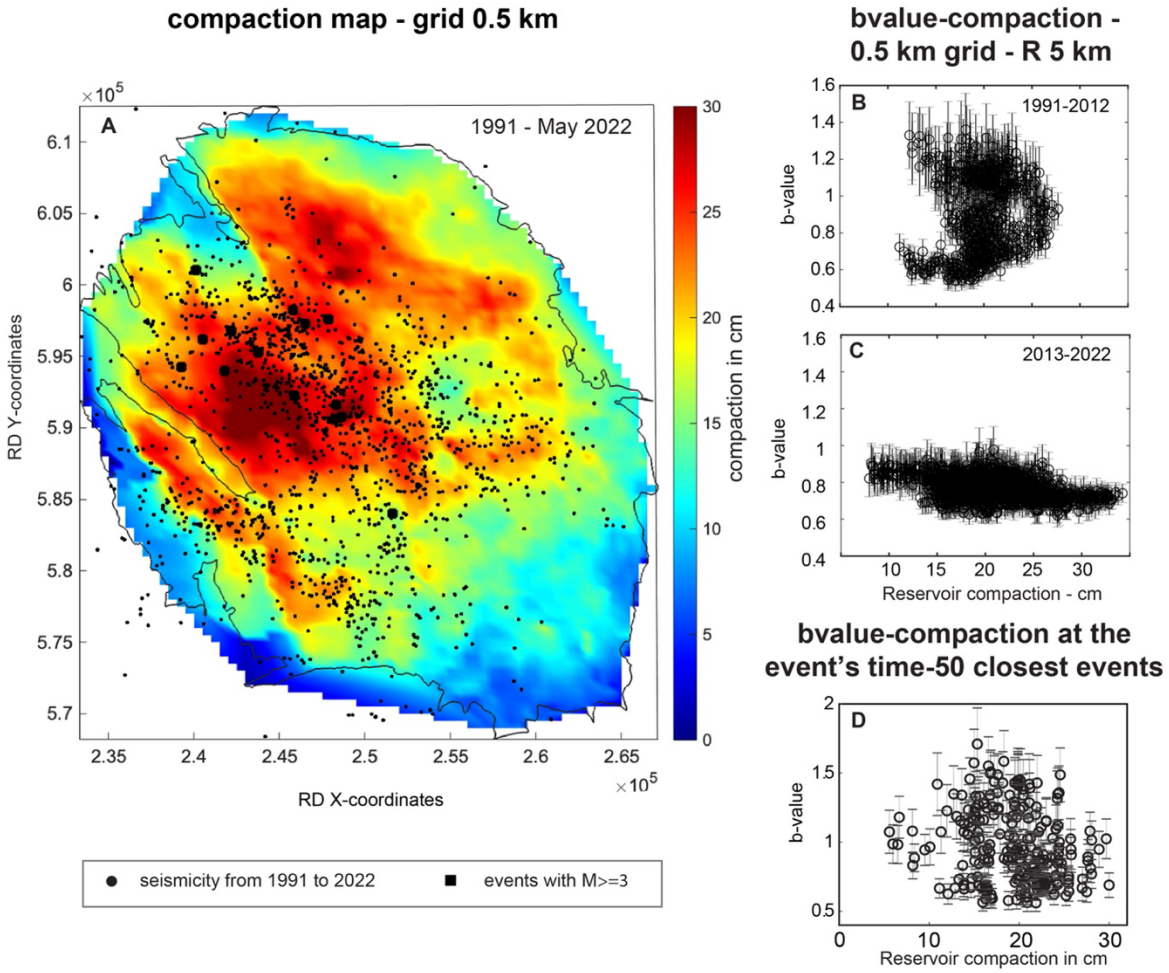

883

884 Figure 9 – ***Compaction map and b-value*** - a) compaction map: cumulative compaction
885 at the year 2022, calibrated on the V6 scenario, operational strategy 2 (OS2; NAM 2021)
886 on a grid of 0.5 km with superimposed seismicity from 1991 to May 2022; b-c) b-value
887 versus compaction for the same 0.5-km spaced grid for the periods 1991-2012 and 2013-
888 2022. Vertical bar: uncertainty by Shi and Bolt (1982); d) b-value calculated for each
889 event in the catalog sampling the closest 50 event above Mc at the origin time versus the
890 compaction of the closest grid node. Vertical bar: uncertainty by Shi and Bolt (1982).

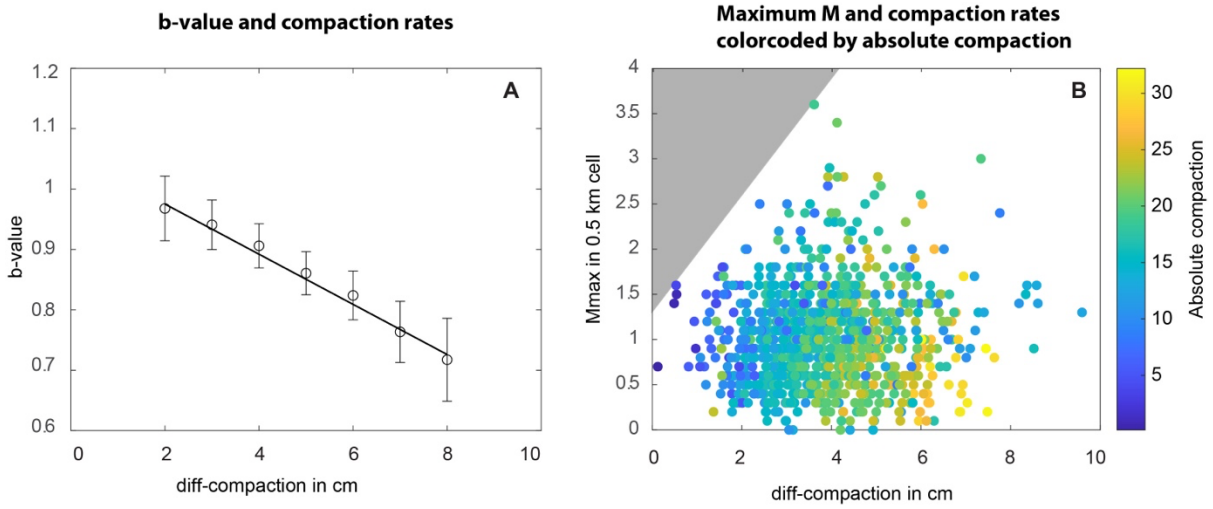

Figure 10 – ***b-value, magnitude, and compaction rates*** - a) Correlation between b-value and compaction rates, expressed by the difference in compaction in 10 years before the event's origin time. Vertical bar: uncertainty by Shi and Bolt (1982); black solid line: linear regression modelling the relationship between b-value and difference in compaction (b=-0.0424x+1.067); b) correlation between the maximum magnitude for each 0.5 km cell and compaction rates, expressed by the difference in compaction in 10 years before the event's origin time, color-coded with respect to the absolute compaction. Gray area: if production does not result in the exceedance of about 0.35 cm of compaction per year, events above M3 do not occur.